



HAL
open science

Extremely strong DLAs at high redshift: gas cooling and H₂ formation

K. N. Telikova, S. A. Balashev, P. Noterdaeme, J. -K. Krogager, A. Ranjan

► **To cite this version:**

K. N. Telikova, S. A. Balashev, P. Noterdaeme, J. -K. Krogager, A. Ranjan. Extremely strong DLAs at high redshift: gas cooling and H₂ formation. *Monthly Notices of the Royal Astronomical Society*, 2022, 510, pp.5974-5983. 10.1093/mnras/stab3800 . insu-03748287

HAL Id: insu-03748287

<https://insu.hal.science/insu-03748287>

Submitted on 6 Jul 2023

HAL is a multi-disciplinary open access archive for the deposit and dissemination of scientific research documents, whether they are published or not. The documents may come from teaching and research institutions in France or abroad, or from public or private research centers.

L'archive ouverte pluridisciplinaire **HAL**, est destinée au dépôt et à la diffusion de documents scientifiques de niveau recherche, publiés ou non, émanant des établissements d'enseignement et de recherche français ou étrangers, des laboratoires publics ou privés.

Extremely strong DLAs at high redshift: gas cooling and H₂ formation

K. N. Telikova¹  , S. A. Balashev¹ , P. Noterdaeme,² J.-K. Krogager^{1,2,3}  and A. Ranjan^{4,2}

¹*Ioffe Institute, Politekhnikeskaya 26, 194021 Saint Petersburg, Russia*

²*Institut d'Astrophysique de Paris, CNRS-SU, UMR 7095, 98 bis bd Arago, F-75014 Paris, France*

³*Department of Astronomy, University of Geneva, Chemin Pegasi 51, CH-1290 Versoix, Switzerland*

⁴*Korea Astronomy and Space Science Institute, 776 Daedeokdae-ro, Yuseong-gu, Daejeon 34055, Korea*

Accepted 2021 December 27. Received 2021 December 20; in original form 2021 September 1

ABSTRACT

We present a spectroscopic investigation with the Very Large Telescope/X-shooter of seven candidate extremely strong damped Lyman- α absorption systems [ESDLAs, $N(\text{H I}) \geq 5 \times 10^{21} \text{ cm}^{-2}$] observed along quasar sightlines. We confirm the extremely high column densities, albeit slightly (0.1 dex) lower than the original ESDLA definition for four systems. We measured low-ionization metal abundances and dust extinction for all systems. For two systems, we also found strong associated H₂ absorption $\log N(\text{H}_2) (\text{cm}^{-2}) = 18.16 \pm 0.03$ and 19.28 ± 0.06 at $z = 3.26$ and 2.25 towards J2205+1021 and J2359+1354, respectively, while for the remaining five we measured conservative upper limits on the H₂ column densities of typically $\log N(\text{H}_2) (\text{cm}^{-2}) < 17.3$. The increased H₂ detection rate (10–55 per cent at 68 per cent confidence level) at high H I column density compared with the overall damped Lyman- α population (~ 5 –10 per cent) confirms previous works. We find that these seven ESDLAs have similar observed properties as those previously studied towards quasars and γ -ray burst afterglows, suggesting they probe inner regions of galaxies. We use the abundance of ionized carbon at the excited fine-structure level to calculate the cooling rates through the C II $\lambda 158 \mu\text{m}$ emission, and compare them with the cooling rates from damped Lyman- α systems in the literature. We find that the cooling rate distribution of ESDLAs also presents the same bimodality as previously observed for the general (mostly lower H I column density) damped Lyman- α population.

Key words: galaxies: high-redshift – galaxies: ISM – quasars: absorption lines.

1 INTRODUCTION

The analysis of the interstellar medium (ISM) of high-redshift galaxies in emission is hampered by the sensitivity limit and spatial resolution of the instruments. Another widely used method for the investigation of the gaseous content of galaxies at high redshifts is to analyse the absorption lines they imprint in the spectra of bright background sources such as γ -ray burst (GRB) afterglows and quasars. In particular, atomic hydrogen manifests itself as characteristic strong Lyman- α H I absorption. Observations of this line with ground-based telescopes are limited to a minimum redshift of $z \approx 1.6$ due to the atmospheric cut-off at $\sim 3200 \text{ \AA}$. For systems with column density $N(\text{H I}) \gtrsim 2 \times 10^{20} \text{ cm}^{-2}$, so-called damped Lyman- α systems (DLAs; see review by Wolfe, Gawiser & Prochaska 2005), hydrogen is predominantly neutral. DLAs have therefore long been considered as regions where star formation processes may potentially occur. Besides H I absorption lines, numerous associated absorption lines from metals at different ionization states are usually detected in DLAs. Moreover, in a small fraction of them, molecules are also found: mostly H₂ (first detected by Levshakov & Varshalovich 1985), but also deuterated molecular hydrogen (first detected by Varshalovich et al. 2001) and CO (first detected by Srianand et al. 2008b). It was shown in simulations (e.g. Rahmati & Schaye 2014) as well as in observations (Noterdaeme et al. 2012a, 2014; Ranjan et al. 2018, 2020) that DLA systems with $N(\text{H I}) \gtrsim 5 \times 10^{21} \text{ cm}^{-2}$,

so-called extremely strong damped Lyman- α (ESDLA) systems, are most likely associated with galaxies at small impact parameters, typically $< 3 \text{ kpc}$, while the rest of the DLA population statistically probes the neutral gas at larger impact parameters (Krogager et al. 2017), most likely associated with the circumgalactic medium. Therefore, investigating ESDLA systems may provide more direct information on galaxy evolution, in particular the physical and chemical conditions and a closer link to star formation in the associated high-redshift galaxies. However, statistical analysis of ESDLA systems is complicated by their small cross-sections, seen in the steep power-law nature of the DLA H I column density distribution: Less than 1 per cent of the DLAs detected in the Sloan Digital Sky Survey (SDSS) (~ 100 systems) have H I column densities larger than $5 \times 10^{21} \text{ cm}^{-2}$ (Noterdaeme et al. 2014). Thereby, detailed analysis of ESDLAs at medium/high spectral resolution has been obtained so far for only about 20 systems towards quasars (e.g. Ranjan et al. 2020, and references therein) and about a dozen systems towards GRB afterglows (Bolmer et al. 2019), where the line of sight pinpoints regions of star formation in galaxies where the burst occurs.

In this work, we present the analysis of seven additional ESDLA systems at $z = 2$ –3 from the same selection as Ranjan et al. (2020), and also obtained with the intermediate-resolution spectrograph X-shooter on the Very Large Telescope (VLT) (Vernet et al. 2011). This paper is organized as follows. In Section 2, we describe the observations and data reduction. In Section 3, we present the analysis of the collected spectra. Finally, we discuss the results and present our summary in Sections 5 and 6, respectively.

* E-mail: k.telikova@gmail.com

Table 1. Log of X-shooter observations.

Quasar	Date	Airmass	Seeing ^a (arcsec)	Exposure time ^b (s)	CNR ^b
J002409.3–072554.8	2018-08-16	1.357	0.83	1490, 1440, 300	22, 12, 8
J123815.9+162043.9	2018-04-09	1.323	0.67	1490, 1440, 300	30, 15, 13
J123815.9+162043.9	2018-04-16	1.328	1.01	1490, 1440, 300	30, 15, 13
J135316.9+095634.8	2018-04-19	1.215	0.85	1490, 1440, 300	20, 14, 11
J141801.9+071846.3	2018-04-23	1.221	0.69	1490, 1440, 300	21, 12, 8
J220525.7+102119.9	2018-07-09	1.232	0.94	1490, 1440, 300	18, 7, 6
J220525.7+102119.9	2018-07-09	1.233	0.89	1490, 1440, 300	20, 8, 6
J235124.8–063916.4	2018-08-11	1.337	1.05	1490, 1440, 300	14, 9, 5
J235124.8–063916.4	2018-08-14	1.348	0.83	1490, 1440, 300	15, 9, 5
J235916.6+135445.0	2018-08-12	1.374	0.78	1490, 1440, 300	18, 13, 13
J235916.6+135445.0	2018-08-15	1.313	1.01	1490, 1440, 300	15, 10, 13

^aCorrected by airmass.

Values for airmass and seeing correspond to the start of the respective exposures.

^bExposure times and typical continuum-to-noise ratios (CNRs) are given for the UVB, VIS, and NIR arms, respectively.**Table 2.** Main derived properties of the ESDLAs.

Quasar	z_{em}^a	z_{abs}	$\log N(\text{H I})$ (cm^{-2})	$\log N(\text{H I})^{\text{SDSS}}$ (cm^{-2})	$\log N(\text{H}_2)$ (cm^{-2})	[X/H]	[Fe/X]	$\log N(\text{Fe}^{\text{dust}})$ (cm^{-2})	A_V^b
J0024–0725	2.87	2.68120	21.81 ± 0.01	21.8	<17.20	$-1.77^{+0.06}_{-0.09}$	$-0.56^{+0.10}_{-0.09}$	$15.40^{+0.12}_{-0.18}$	<0.1
J1238+1620	3.43	3.20907	21.60 ± 0.01	21.7	<17.25	$-1.01^{+0.05}_{-0.05}$	$-0.43^{+0.06}_{-0.05}$	$15.89^{+0.13}_{-0.16}$	<0.1
J1353+0956	3.61	3.33326	21.61 ± 0.01	21.7	<17.30	$-1.61^{+0.13}_{-0.20}$	$-0.46^{+0.22}_{-0.15}$	$15.32^{+0.22}_{-0.61}$	<0.1
J1418+0718	2.58	2.39211	21.59 ± 0.02	21.8	<17.20	$-1.50^{+0.05}_{-0.04}$	$-0.36^{+0.05}_{-0.06}$	$15.34^{+0.13}_{-0.15}$	<0.1
J2205+1021	3.41	3.25516	21.61 ± 0.02	21.7	18.16 ± 0.03	$-0.93^{+0.05}_{-0.05}$	$-0.87^{+0.09}_{-0.07}$	$16.12^{+0.09}_{-0.10}$	<0.1
J2351–0639	2.91	2.55744	21.90 ± 0.01	21.9	<17.75	$-1.58^{+0.05}_{-0.05}$	$-0.46^{+0.11}_{-0.11}$	$15.64^{+0.13}_{-0.17}$	<0.1
J2359+1354	2.77	2.2499	21.96 ± 0.02	22.0	19.28 ± 0.06	$-0.47^{+0.03}_{-0.03}$	$-0.94^{+0.03}_{-0.03}$	$16.94^{+0.23}_{-0.37}$	0.3

^aQuasar redshift.^bThe upper limits on A_V correspond to the systems for which the obtained extinction is less than the systematic uncertainty (≤ 0.1) due to dispersion of intrinsic spectral shapes of quasars.

'X' refers to a volatile element, which is zinc for all ESDLAs but that towards J1418+0718, for which X is sulphur; see text.

2 OBSERVATIONS AND DATA REDUCTION

The ESDLA candidates were taken from the parent SDSS Data Release 14 (SDSS-DR14; Abolfathi et al. 2018) DLA sample with the conditions to be observable from Paranal in a reasonable amount of observing time. A first set of data was published by Ranjan et al. (2020) and the remaining were prepared for observations based on best observability during the allocated period. Observations were carried out in 2018 under Program ID 0101.A-0891(A) (PI: Ranjan) in service mode with the intermediate-resolution multiwavelength spectrograph X-shooter mounted on the European Southern Observatory Very Large Telescope Unit 2 (Kueyen). Observations were obtained with the nodding mode using a nod throw of 4 arcsec and slit widths of 1.6, 0.9, and 1.2 arcsec for the UVB, VIS, and NIR arms, respectively. The UVB and VIS detectors were read out using 1×2 binning. The data were processed using the EsoRex pipeline version 2.6.8 specifically designed to combine exposures with nodding offsets along the slit (Goldoni et al. 2006; Modigliani et al. 2010). All spectra were flux calibrated using observations of a spectroscopic standard star taken on the same night as the respective science target. For four targets, we obtained two separate observations that were individually processed and subsequently combined using an inverse-variance-weighted combination. The 1D spectra were then extracted from the combined observations following the steps of the optimal extraction algorithm (Horne 1986). Wavelengths were converted to

vacuum and expressed in the heliocentric rest frame. Finally, the spectra were corrected for Galactic extinction using the dust maps of Schlafly & Finkbeiner (2011). Since we do not analyse any features in regions of strong telluric absorption, the spectra have not been corrected for telluric absorption.

Since the observations were performed under good seeing conditions, throughout the analysis, we have used a nominal spectral resolution in the UVB, VIS, and NIR arms of 5400, 8900, and 5600, respectively, corresponding to the smaller slit widths, which matches the average seeing. Observational details are presented in Table 1.

3 SPECTROSCOPIC ANALYSIS

We analysed the absorption lines using standard multicomponent Voigt-profile fitting procedures (for the details, see Balashev et al. 2019). A summary of the main properties of the ESDLAs analysed here is presented in Table 2. Details on the absorption-line analysis are provided in the subsequent subsections with the corresponding table parameters and figures presented as a supplementary material.

3.1 Neutral atomic hydrogen

We estimated the H I column densities through fitting Ly-series lines (in most cases Ly α and Ly β) with a one-component Voigt-profile model. Since extremely strong damped Ly α lines absorb the

quasar continuum over a wide wavelength range, the widely used method of continuum reconstruction by eye can be significantly biased. In turn, we modelled the continuum at the location of Ly α lines using Chebyshev polynomials,¹ whose parameters were fitted simultaneously with profiles of H I absorption lines. As an initial guess of the unabsorbed quasar continuum, we first used the visual estimation aided by a B-spline interpolation. In the high-column-density regime, the derived column densities are actually insensitive to the choice of the Doppler parameter b . Therefore, we fixed b with a value chosen to roughly reproduce the width of the observed high Lyman series lines. Fit profiles to the H I Ly α absorption lines are shown in Fig. 1. Although the estimated H I column densities are consistent with the values measured from the low-signal-to-noise-ratio, low-resolution spectra from the SDSS (Noterdaeme et al. 2012c, 2014), four systems (J1238+1612, J1353+0956, J1418+0718, and J2205+1021) have H I column densities ~ 0.1 dex below the threshold originally used to define ESDLAs [$N(\text{H I}) \geq 5 \times 10^{21} \text{ cm}^{-2}$]. For the sake of simplicity, we continue calling them ESDLAs in the following.

3.2 Molecular hydrogen

We searched for resonant rest-frame UV H₂ absorption lines, i.e. lines in the Lyman and Werner bands. For two systems, towards J2205+1021 and J2359+1354, we firmly detected strong H₂ absorption with total column densities $\log N(\text{H}_2) (\text{cm}^{-2}) = 18.16 \pm 0.03$ and $\log N(\text{H}_2) (\text{cm}^{-2}) = 19.28 \pm 0.06$, respectively. For the remaining five systems, there are no obvious H₂ signatures detectable in the X-shooter spectra. Therefore, we estimated conservative upper limits on H₂ column densities, focusing on the $J = 0$ and $J = 1$ rotational levels that are known to contain most of the total column density. We used a method similar to that described by Ranjan et al. (2020). We fixed the Doppler parameter b to 1 km s^{-1} and the T_{01} temperature to 100 K, and created synthetic profiles at redshift that varied within the range that corresponds to the observed velocity extent of the metal lines (typically $100\text{--}200 \text{ km s}^{-1}$). Due to presence of a Ly α forest in the H₂ absorption region, we focused only on the positive residuals. The upper limit of the $N(\text{H}_2)$ is obtained as the largest column density for which the synthetic profile remains consistent with the observed spectrum with the corresponding fraction of positive residuals above 2σ level less than 5 per cent. Constraints on the total $N(\text{H}_2)$ are presented in Table 2. In Fig. 2, we provide the H I–H₂ diagram for the DLAs detected at $z \gtrsim 2$. Our measurements of H₂ column densities result in an incidence rate of H₂ of 10–55 per cent based on the binomial proportion interval at 68 per cent confidence level in agreement with that obtained from ESDLAs towards quasars, ~ 40 per cent (Balashev & Noterdaeme 2018; Ranjan et al. 2020), as well as from GRB afterglows, ~ 30 per cent (Bolmer et al. 2019). Although here we have only upper limits on H₂ column densities for five out of seven systems, our results confirm a higher H₂ incidence rate for high H I column density systems compared with the overall DLA population, $\sim 5\text{--}10$ per cent (Balashev & Noterdaeme 2018).

3.3 Metal column densities and dust depletion

The main purpose of the current work is the derivation of the chemical and physical conditions in the neutral phase of the absorbing gas.

¹The order of polynomial was defined based on the wavelength range and usually was 6–8.

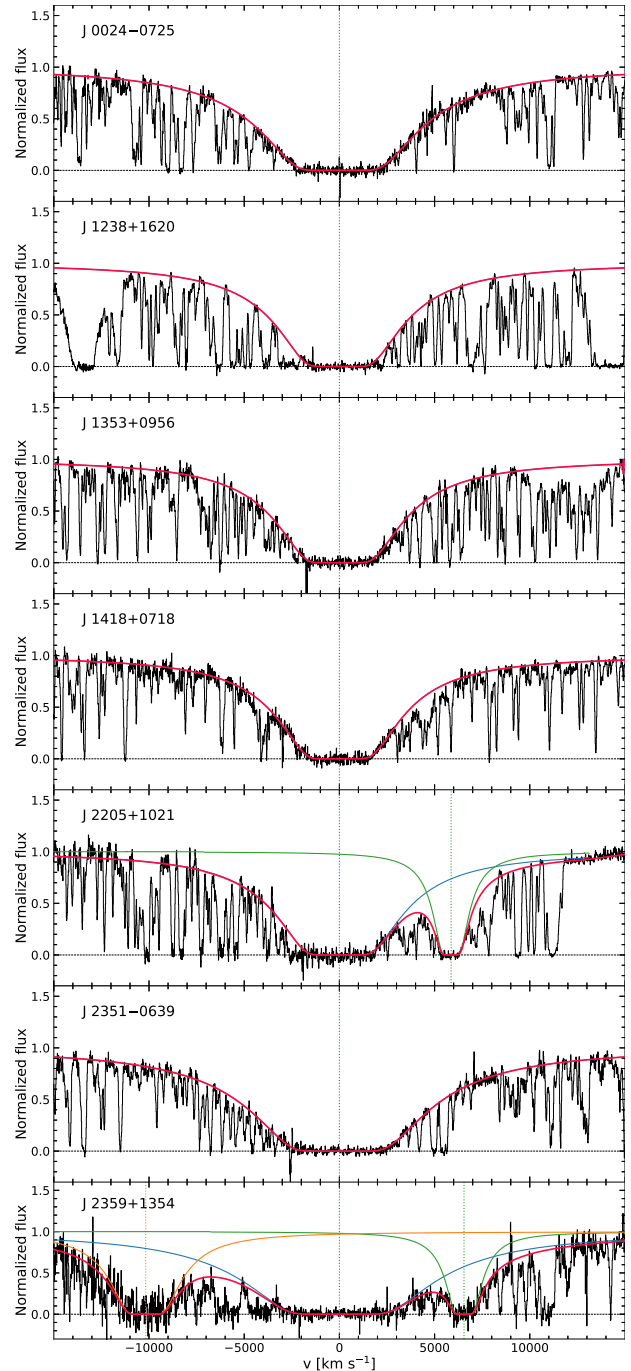


Figure 1. Fit to the H I Ly α profiles of ESDLAs in the sample. Black and red lines show the observed spectrum and total fit profiles, respectively. The blue solid line indicates the profile of studied ESDLA, while the green and orange lines correspond to additional fitted damped Ly α transitions. The x -axis indicates the relative velocity with respect to the ESDLA redshifts.

Consequently, we focus on the low-ionization metal species (with ionization potential $< 13.6 \text{ eV}$) such as Si II, Zn II, Cr II, S II, Fe II, Mn I, Ni II, Ti II, O I, C I, and C II. All species, except C I, which is more likely associated with molecular gas, were fitted using a common b parameter and velocity structure. Throughout the paper, we calculate metal abundances with respect to solar ones (from

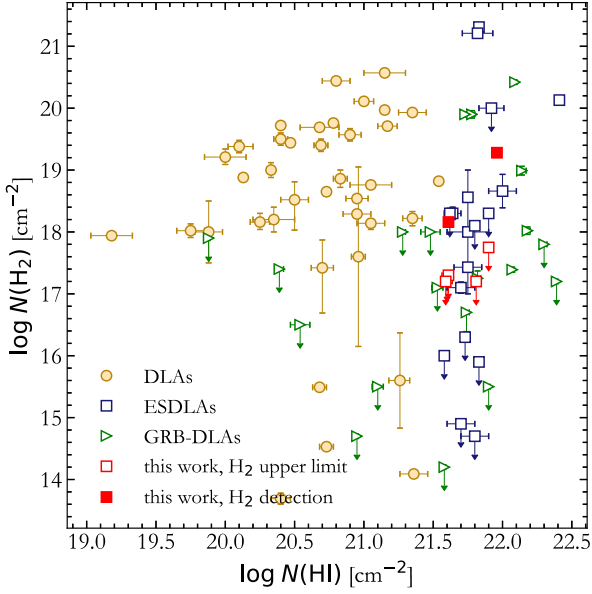


Figure 2. H I versus H₂ column densities. ESDLAs from this work are shown by open (H₂ upper limits) and filled (H₂ detections) red squares. Blue squares and brown circles are ESDLAs and DLAs from Ranjan et al. (2018, 2020), Noterdaeme et al. (2007a, 2008a,b, 2010, 2014, 2015, 2018), Guimarães et al. (2012), Fynbo et al. (2011), Rahmani et al. (2013), Ellison et al. (2001), Klimenko et al. (2015), Balashev, Ivanchik & Varshalovich (2010), Balashev et al. (2011, 2017, 2019), Albornoz Vásquez et al. (2014), Carswell et al. (2011), Srianand et al. (2010), Jorgenson, Wolfe & Prochaska (2010), Milutinovic et al. (2010), and Krogager et al. (2016). GRB DLAs from Bolmer et al. (2019) are shown by triangles.

Asplund et al. 2009) as²

$$[X/H] = \log \left(\frac{N(X)}{N(H)} \right) - \log \left(\frac{X}{H} \right)_{\odot} \quad (1)$$

and

$$[Fe/X] = \log \left(\frac{N(Fe II)}{N(X)} \right) - \log \left(\frac{Fe}{X} \right)_{\odot}. \quad (2)$$

Both sulphur and zinc are known to be volatile species that deplete little into dust (e.g. Vladilo et al. 2000). We hence estimated the metallicities and dust depletion factors using zinc-to-hydrogen and iron-to-zinc ratios for all systems except J1418+0718, for which we used sulphur instead of zinc, owing to the better constraint on S II than on Zn II for this system. The sixth column of Table 2 presents these metallicities only, but detailed abundances are provided for each system as a supplementary material.

Since the production and shielding of H₂ is intimately linked to the dust content, we assume an intrinsic solar abundance pattern and estimate the column density of iron locked into the dust from the observed column densities as

$$N(Fe^{dust}) = (1 - 10^{[Fe/X]})N(X) \left(\frac{Fe}{X} \right)_{\odot}, \quad (3)$$

where X again refers to zinc (sulphur for J1418+0718).

²For our seven ESDLAs, $N(H) = N(H I) + 2N(H_2) \approx N(H I)$, since $\log N(H_2) (\text{cm}^{-2}) < 19.3$.

3.4 [C II] cooling rate

The fine-structure [C II] $\lambda 158 \mu\text{m}$ transition from the collisionally excited $^2P_{3/2}^{\circ}$ level (e.g. Goldsmith et al. 2012) is a key contributor to the cooling of the cold ISM (e.g. Lagache, Cousin & Chatzikos 2018). Instead of direct [C II] $\lambda 158 \mu\text{m}$ emission, one can estimate the ISM cooling rate l_c locally (per unit hydrogen atom) in absorption, by measuring the column density of ionized carbon in its first excited level $N(\text{C II}^*)$ through its electronic transition at 1335 Å (Pottasch, Wesselius & van Duinen 1979; Wolfe, Prochaska & Gawiser 2003):

$$l_c = \frac{N(\text{C II}^*)h\nu_{ul}A_{ul}}{N(\text{H I})} \text{ erg s}^{-1} \text{ H}^{-1}, \quad (4)$$

where $A_{ul} = 2.29 \times 10^{-6} \text{ s}^{-1}$ is the Einstein coefficient for the spontaneous decay $^2P_{3/2}^{\circ} \rightarrow ^2P_{1/2}^{\circ}$ and $h\nu_{ul}$ is the energy of this transition. It was possible to constrain the C II* column densities for three systems in our X-shooter sample (towards J0024–0725, J1353+0956, and J1418+0718), while the C II* absorption is strongly saturated for the remaining four. To enrich this sample, we also estimated C II* column densities in the ESDLA sample from Ranjan et al. (2020). In total, we derived the [C II] cooling rates for seven ESDLAs obtained with X-shooter and four ESDLAs obtained with UVES (Dekker et al. 2000) (see Table 3). For ESDLAs detected in X-shooter spectra, we cannot exclude saturation of the C II* absorption, since the velocity structure is likely unresolved. Therefore, we obtained a conservative interval estimate on the C II* column density using two limiting cases. As a lower limit of $\log N(\text{C II}^*)$, we used measurement obtained by the simultaneous fit of the C II* absorption line with other metal lines in the system. These lower limits correspond to the optically thin or intermediate saturation of C II* lines. To obtain conservative upper limits on $N(\text{C II}^*)$, we fitted C II* lines using a one-component profile with the Doppler parameter $b = 3 \text{ km s}^{-1}$ as more robustly derived at high resolution. As a point estimate for further calculations [except for J1349+0448, for which we provide only a lower limit to $N(\text{C II}^*)$], we use the mean column density of the obtained $N(\text{C II}^*)$ range. The quoted uncertainties in Table 3 correspond to this conservative range. In Fig. 3, we compare the derived [C II] cooling rates of ESDLAs with those of DLAs from Wolfe et al. (2008)³ and Dutta et al. (2014). Our results tend to support the bimodality in the [C II] cooling rate distribution previously observed by Wolfe et al. (2008) with the following two groups of DLAs: *high* $\log l_c (\text{erg s}^{-1} \text{ H}^{-1}) > -27$ and *low* $\log l_c (\text{erg s}^{-1} \text{ H}^{-1}) \lesssim -27$. Indeed, four ESDLAs in our sample have *low* cooling rates of $\log l_c (\text{erg s}^{-1} \text{ H}^{-1}) \sim -27.2$, while six have *high* cooling rates of $\log l_c (\text{erg s}^{-1} \text{ H}^{-1}) \sim -26.5$. To quantitatively test whether or not our systems contradict the statistical properties previously obtained for the overall DLAs, we use a Gaussian mixture algorithm with two components, as done by Wolfe et al. (2008), but applying it to the whole DLA plus ESDLA sample. We obtained two groups of cooling rates with median $\log l_c (\text{erg s}^{-1} \text{ H}^{-1}) = -26.6$ and -27.3 with the corresponding fraction of systems being 0.6 and 0.4, respectively.

For all the ESDLA systems in our sample, observed with UVES, that is where the velocity structure is easily resolved and saturation of the lines can be easily assessed, we measure *high* cooling rates, while four of six X-shooter ESDLAs fall in the *low*-cooling-rate group. It is legitimate to wonder whether this difference in ESDLA cooling

³For several systems in Table 1 from Wolfe et al. (2008), which have zero uncertainties on $\log N(\text{H I})$, we use a value of 0.1 dex for uncertainty on $\log N(\text{H I})$. These values correspond to the uncertainties typically measured using high-resolution spectra and are consistent with the error bars shown in fig. 1 in Wolfe et al. (2008).

Table 3. Fine-structure excitation of ionized carbon and derived cooling rates.

Quasar	$\log N(\text{H I})$ (cm^{-2})	$\log N(\text{H}_2)$ (cm^{-2})	$\log f^a$	[X/H]	$\log N(\text{C II}^*)$ (cm^{-2})	$\log l_c$ ($\text{erg s}^{-1} \text{H}^{-1}$)	Instrument	Refs ^b
J0024–0725	21.81 ± 0.01	< 17.20	< -4.30	$-1.77^{+0.06}_{-0.09}$	13.93 ± 0.35	-27.42 ± 0.35	XS	1
J1353+0956	21.61 ± 0.01	< 17.30	< -4.00	$-1.61^{+0.13}_{-0.20}$	14.07 ± 0.50	-27.08 ± 0.50	XS	1
J1418+0718	21.59 ± 0.02	< 17.20	< -4.07	$-1.50^{+0.05}_{-0.04}$	13.87 ± 0.29	-27.26 ± 0.29	XS	1
J0017+1307	21.62 ± 0.03	< 18.3	< -2.99	-1.50 ± 0.09	14.76 ± 0.88	-26.40 ± 0.88	XS	2
J1349+0448	21.80 ± 0.01	< 18.1	< -3.39	-1.35 ± 0.06	> 14.16	> -27.17	XS	2
J2232+1242	21.75 ± 0.03	18.56 ± 0.02	-2.89 ± 0.03	-1.48 ± 0.05	14.83 ± 0.76	-26.46 ± 0.76	XS	2
J2322+0033	21.58 ± 0.03	< 16.0	< -5.25	-1.71 ± 0.13	14.06 ± 0.45	-27.06 ± 0.45	XS	2
HE 0027–1836	21.75 ± 0.10	17.43 ± 0.02	$-4.02^{+0.10}_{-0.04}$	-1.59 ± 0.10	$14.67^{+0.13}_{-0.09}$	$-26.62^{+0.16}_{-0.13}$	UVES	4
J0843+0221	21.82 ± 0.11	21.21 ± 0.02	$-0.48^{+0.07}_{-0.08}$	$-1.52^{+0.08}_{-0.10}$	$14.91^{+0.28}_{-0.17}$	$-26.45^{+0.30}_{-0.19}$	UVES	3
Q 1157+0128	21.80 ± 0.10	< 14.75	< -6.65	-1.40 ± 0.10	14.7 ± 0.02	-26.59 ± 0.10	UVES	5
J2140–0321	22.41 ± 0.03	20.13 ± 0.07	-1.98 ± 0.06	-1.52 ± 0.08	$15.63^{+0.46}_{-0.47}$	$-26.32^{+0.46}_{-0.46}$	UVES	2

^a $f = 2N(\text{H}_2)/[2N(\text{H}_2)+N(\text{H I})]$ is molecular fraction.

^bReferences correspond to the H I and H₂ column density measurements: (1) this work, (2) Ranjan et al. (2020), (3) Balashev et al. (2017), (4) Noterdaeme et al. (2007b), and (5) Noterdaeme et al. (2008a).

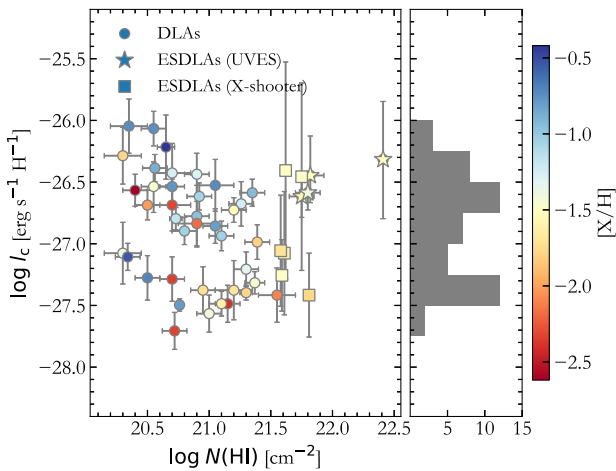


Figure 3. [C II] cooling rates versus H I column densities. Circles correspond to the DLAs from Wolfe et al. (2008, and references therein) and Dutta et al. (2014). Stars and squares are the ESDLAs from this work, obtained with UVES and X-shooter, respectively. Colours encode the metallicity. The histogram corresponds to the cooling rate distribution, marginalized over the H I column densities.

rates arises from the use of two instruments. However, even our conservative procedure for the $N(\text{C II}^*)$ upper limit rules out high saturation of the C II* lines (see Table 3). Therefore, the provided interval estimation of the $N(\text{C II}^*)$ for X-shooter systems is quite robust. In addition, the difference in the cooling rates of the X-shooter and UVES ESDLAs in our sample is supported by the coincidentally higher H₂ abundance in the ESDLAs studied with UVES than in those studied with X-shooter.

Wolfe et al. (2008), under the assumption that heating through photoelectric effect equates [C II] cooling, suggested that the bimodality in [C II] cooling rates originates from a mass transition in a galaxy formation scenario and corresponds to different star formation regimes. Recently, Roy et al. (2017) argued that inferring the star formation rate from C II* is not straightforward due to the presence of C II* in both the warm neutral medium (WNM) and the cold neutral medium (CNM). The authors stressed the absence of evident correlation between $N(\text{C II}^*)$ and the H I column density in each of these two phases in the Galaxy. This means that the

two-phase origin of C II* absorption must be taken into account. Moreover, [C II] $\lambda 158 \mu\text{m}$ emission is the main coolant only for the cold phase of neutral ISM, while the cooling of the warm phase is dominated by Ly α emission, which sets the WNM temperature of $\sim 10^4$ K (as robustly derived in several DLAs; see e.g. Carswell et al. 2012; Cooke, Pettini & Jorgenson 2015; Noterdaeme et al. 2012b, 2021b). Therefore, assuming dominant [C II] cooling and thermal balance to derive the heating rate and hence the star formation is only possible when most of the C II* arises from the cold phase with temperatures greater than a few hundred kelvins.

Interestingly, the consistent bimodality in the l_c distribution observed in our sample of ESDLAs does not comply with the explanation by Wolfe et al. (2008) of its origin in DLA samples. Wolfe et al. (2008) argued that the bimodality arises from a difference in star formation regimes for two distinct galaxy populations: more massive metal-rich and less massive metal-poor systems. However, our C II*-selected ESDLA sample is quite homogeneous in terms of metallicities ($[\text{X}/\text{H}] \sim -1.5$; see Table 3) and Si II $\lambda 1526$ equivalent widths (which were used by Wolfe et al. as a mass indicator). The selection of ESDLAs is also more homogeneous in terms of the galactic environment that the line of sight traverses compared with that of DLAs, since ESDLAs are more likely to probe galaxies at low impact parameters, while DLAs probe predominantly the interface between interstellar and circumgalactic gas at larger impact parameters.

As an alternative explanation, we suggest that the l_c bimodality is more likely due to the phase separation of the neutral ISM rather than a bimodality in the star formation regimes. We address this issue quantitatively in the work Balashev, Telikova & Noterdaeme (2022) and show that the bimodality originates in the C II*/C II-metallicity plane and can be naturally explained by the phase separation in the ISM and the dependence of their characteristic number densities on metallicity.

3.5 Electron density

Far from ionizing sources, the collisional excitation of C II* and Si II* dominates over the radiative excitation and C II* and Si II* column densities may be used to estimate the electron density assuming equilibrium between collisional excitation and spontaneous radiative de-excitation (Srianand & Petitjean 2000). For the system at $z = 2.2486$ towards J2359+1354 with the highest H I column density,

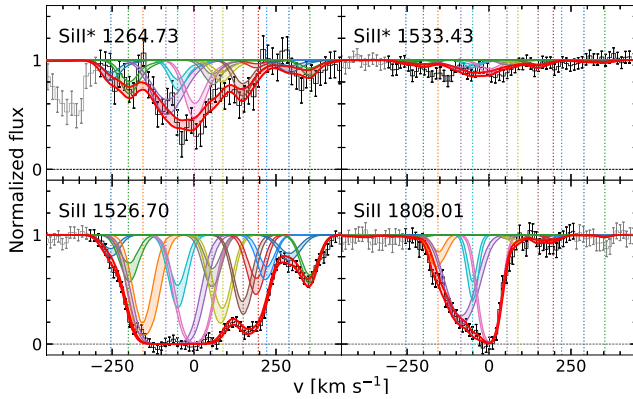


Figure 4. Fit to Si II and Si II* lines in J2359+1354. The red regions indicate the total Voigt profiles with corresponding 1σ uncertainties. The vertical dashed lines correspond to the relative positions of the individual fit components.

we detected Si II* absorption via Si II* 1264 and 1533 Å transitions, which were fitted simultaneously with Si II and other available metal specie. The line profiles of Si II and Si II* transitions are shown in Fig. 4. Although these lines are partially blended, we obtained a total $\log N(\text{Si II}^*) (\text{cm}^{-2}) = 13.84^{+0.04}_{-0.03}$ that translates into $N(\text{Si II}^*)/N(\text{Si II}) = (1.0^{+0.1}_{-0.2}) \times 10^{-3}$. This value is in agreement with what was measured towards J1135–0010 by Kulkarni et al. (2012), but ten times higher than what was measured in two other ESDLAs (Noterdaeme et al. 2015; Balashev et al. 2017). Excited Si II fine-structure levels can be populated either by collisions with atomic (and molecular) hydrogen in a mostly neutral medium or by collisions with electrons in an ionized phase surrounding the pockets of neutral gas. However, since the measured $N(\text{Si II}^*)/N(\text{Si II})$ ratio is relatively high, it would require very high thermal pressures of $\sim 10^6 \text{ K cm}^{-3}$ if the collisions were dominated by neutral species for both warm atomic and cold molecular phases. Therefore, we suggest that Si II* is mostly associated with the ionized gas, where it is efficiently populated by electrons. In case of the equilibrium between collisional excitation and spontaneous radiative de-excitation for Si II, the electron number density n_e can be expressed as a function of the gas temperature as

$$n_e = \frac{A_{21}}{C_{12}(T)} \frac{N(\text{Si II}^*)}{N(\text{Si II})}, \quad (5)$$

where $A_{21} = 2.13 \times 10^{-4} \text{ s}^{-1}$ is the Einstein coefficient for the spontaneous decay for Si II* and $C_{12} = 3.32 \times 10^{-5} T^{-0.5} \exp(-413.4/T) \text{ cm}^3 \text{ s}^{-1}$ is the temperature-dependent collisional excitation rate for Si II (e.g. Srianand & Petitjean 2000). Assuming a temperature of $\sim 10^4 \text{ K}$, we obtain an electron number density of $n_e \sim 0.7 \text{ cm}^{-3}$. This should be considered as a lower limit to the electron density in the ionized medium, since we do not know how much of the observed Si II column density is associated with this phase. Hence, the actual $N(\text{Si II}^*)/N(\text{Si II})$ ratio in the ionized medium can be higher (see also Noterdaeme et al. 2021a).

3.6 Neutral carbon

We searched for the presence of neutral carbon C I lines in our X-shooter spectra of ESDLAs since this species is known to be a good tracer of molecular hydrogen (e.g. Srianand et al. 2005; Noterdaeme et al. 2018). We detected C I absorption lines only in the system towards J2359+1354, i.e. the absorber with the highest H_2 column density and dust extinction. The Doppler parameter and redshift for

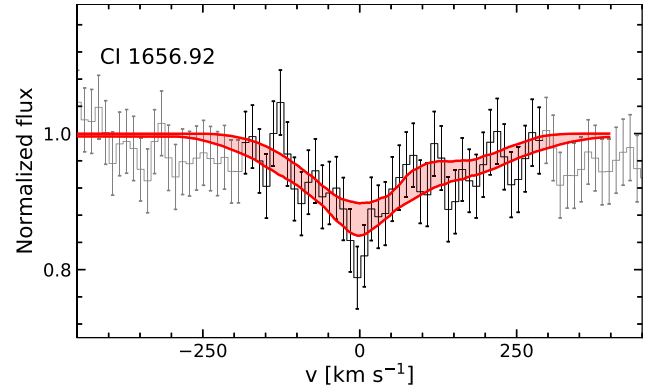


Figure 5. Fit to C I lines in J2359+1354. The red region indicates the joint profile with the corresponding 1σ uncertainty of the mutually blended C I transitions around 1656 Å from the three fine-structure levels. The x-axis shows the relative velocity with respect to the C I $J = 0$ transition.

the C I lines were varied during the one-component fit independently from the low-ionization metals. We measured $\log N(\text{C I}^{01}) (\text{cm}^{-2}) = 13.72 \pm 0.06$ at $z = 2.2485$ from fitting the transitions C I, C I*, and C I** at $\sim 1656 \text{ Å}$, see Fig. 5. Unfortunately, other C I lines are strongly blended. This total column density is similar to what is seen in other H_2 -bearing DLAs (e.g. Klimenko & Balashev 2020).

3.7 Dust extinction

We estimated the extinction due to the presence of dust in the intervening absorption system by fitting the observed spectrum with a quasar template spectrum shifted to the respective quasar emission redshift and reddened with the empirical extinction law for the Small Magellanic Cloud (SMC; Gordon et al. 2003) applied at z_{abs} (see e.g. Srianand et al. 2008a). We used the X-shooter composite spectrum by Selsing et al. (2016) as a reference for the unabsorbed quasar spectrum (except for J1353+0956, for which we used a composite spectrum from *Hubble Space Telescope* data by Telfer et al. 2002). We caution that systematic uncertainties prevail over the statistical ones due to the unknown intrinsic shape of the quasar continuum. Therefore, we present in this paper only systematic errors of the A_V , estimated from the typical dispersion of intrinsic shapes of quasars (see e.g. Noterdaeme et al. 2017; Ranjan et al. 2020). For six out of seven quasars, the measured extinction is compatible with the systematic uncertainties. However, for the system with the highest metallicity and H_2 column density, namely J2359+1354, the estimated extinction is statistically significant $A_V \approx 0.3$, see Fig. 6. This value is in agreement with the measurements of dust extinction for C I-selected systems from Zou et al. (2018) with mean $A_V \approx 0.2$, as well as with the overall A_V - $N(\text{Fe}^{\text{dust}})$ trend obtained for both local and high-redshift ISM (e.g. Zou et al. 2018). Additionally, we estimated the extinction by scaling with metallicity the gas-to-dust ratio, obtained for the Milky Way from X-ray absorption of the GRB afterglows (Watson 2011):

$$A_V^{\text{scale}} = 3.0 \times 10^{-22} \text{ cm}^2 N(\text{H I}) 10^{[\text{Zn}/\text{H}]} (1 - 10^{[\text{Fe}/\text{Zn}]}) \quad (6)$$

In equation (6), we implicitly take into account that the metallicity from Anders & Grevesse (1989) used to derive the relation by Watson (2011) is ~ 1.5 times higher than that from Asplund et al. (2009), which is used in this paper. Applying this equation to our sample, we get typical values of $A_V^{\text{scale}} \lesssim 0.1$, i.e. below the detection limit and hence in agreement with spectral measurements, with the exception

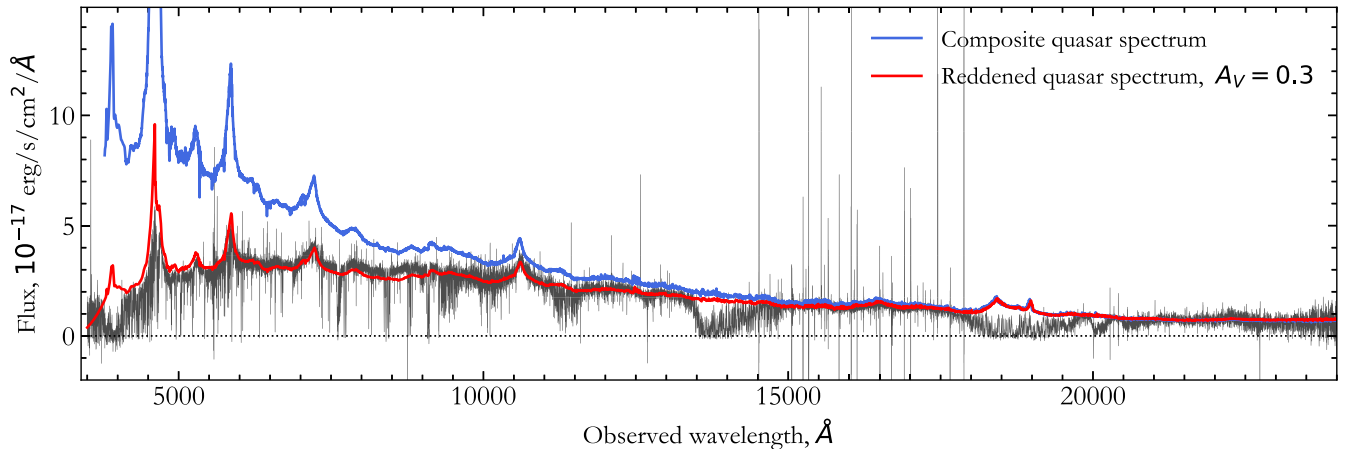


Figure 6. Measurement of dust extinction towards the quasar J2359+1354. The observed X-shooter spectrum is shown in black and matched using a quasar composite spectrum from Selsing et al. (2016) reddened with the SMC extinction law at $z_{\text{abs}} = 2.25$ with the best-fitting value $A_V = 0.3$ (red). For comparison, the unreddened quasar composite spectrum is shown in blue.

of the ESDLA towards J2359+1354, where we obtain $A_V^{\text{scale}} \sim 0.8$. This value is higher than the extinction estimated directly from the spectrum, $A_V \approx 0.3$. The reason for such a disagreement could be a difference in the gas-to-dust ratios for the SMC and the Milky Way.

4 EMISSION LINES

Since ESDLAs are likely arising from gas at small galactocentric radii (Ranjan et al. 2020), we have searched for their emission counterparts. We searched for [O II] $\lambda 3727$ and [O III] $\lambda 5007$. We did not include H α as it is either not covered by our NIR spectra or located at the very noisy end of our spectra. We also only considered the final combined spectra as the data were obtained using nodding along the slit. Hence, all spatial information along the slit is lost and we only consider the region close to the quasar within 7 pixels above and below the spectral trace (corresponding to ± 1.5 arcsec). For each line, we first subtracted the spectral point spread function (SPSF) of the quasar in order to search for faint emission lines from the foreground absorbing galaxy. To this end, we created an empirical SPSF model by median combining the spatial profile of the spectral trace in two regions⁴ on both sides of the expected position of the given emission line.

Next, we median filtered and fitted a third-order polynomial to the peak flux of the observed spatial profile as a function of wavelength. This provided us with a smooth function for the peak flux density as function of wavelength, $I_{\text{max}}(\lambda)$. The empirical SPSF generated above was then rescaled to the peak flux density for a given wavelength, determined by $I_{\text{max}}(\lambda)$ before being subtracted from the observed spatial profile at the given wavelength.

The result is a quasar-subtracted cut-out around each expected emission line. One example is shown in Fig. 7. We do not observe any clear emission lines at the expected relative velocities for O II $\lambda 3727$ and O III $\lambda 5007$. For J1418+0718, we see some tentative evidence for a faint emission peak at ~ 90 km s⁻¹. However, the line is in a region of rather bright sky emission lines, and should be considered highly uncertain. Both emission lines for J0024–0725 fall in regions of very strong and saturated telluric absorption lines, which are not possible to correct, and will therefore not be considered further.

⁴In total, we averaged over relative velocities from 800 to 2400 km s⁻¹ on either side.

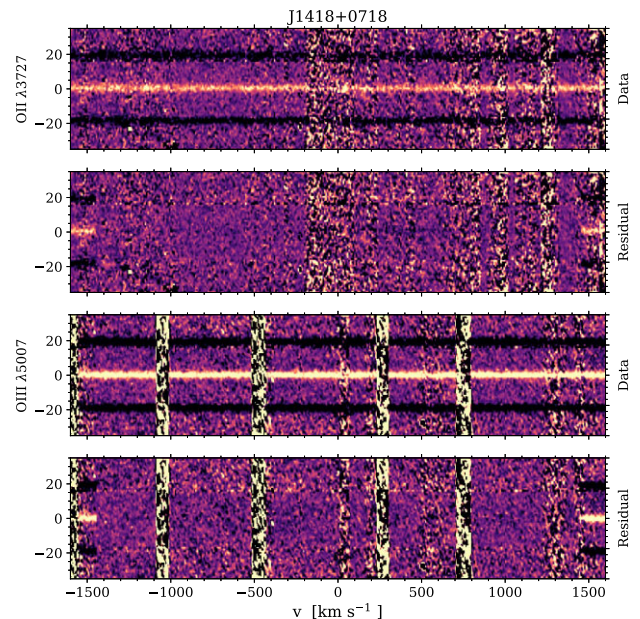


Figure 7. Cut-outs of O II $\lambda 3727$ and O III $\lambda 5007$ emission regions from the 2D spectrum of the system towards J1418+0718 without (data) and with (residual) subtracted quasar trace.

We hence measured upper limits on the emission line fluxes using 500 random apertures displaced along the dispersion axis within ± 250 km s⁻¹ and within ± 3 pixels along the spatial axis. Each aperture is a rectangular box 400 km s⁻¹ wide and $2 \times$ spatial full width at half-maximum ($\text{FWHM}_{\text{spatial}}$) high. The $\text{FWHM}_{\text{spatial}}$ is measured from the model SPSF itself. For our targets, the $\text{FWHM}_{\text{spatial}}$ is in the range of 2–3 pixels (at a scale of 0.21 arcsec per pixel). The upper limits are quoted at 3σ using the standard deviation of the distribution of individual aperture fluxes. The limits on line fluxes and estimated star formation rates based on O II $\lambda 3727$ are summarized in Table 4. The constraints on the star formation rates are in agreement with those of the ESDLAs with detected emission counterparts (Møller, Fynbo & Fall 2004; Kulkarni et al. 2012; Noterdaeme et al. 2012a; Ranjan et al. 2020).

Table 4. Summary of line flux measurements.

Quasar	$F([\text{O II}] \lambda 3727)$ ($\text{erg s}^{-1} \text{cm}^{-2}$)	SFR ^a ($M_{\odot} \text{yr}^{-1}$)	$F([\text{O III}] \lambda 5007)$ ($\text{erg s}^{-1} \text{cm}^{-2}$)
J 0024–0725	$<4.4 \times 10^{-17}$	<24	$<9.7 \times 10^{-17}$
J 1238+1620	$<8.7 \times 10^{-18}$	<7	$<1.7 \times 10^{-16}$
J 1353+0956	$<2.3 \times 10^{-17}$	<21	$<1.2 \times 10^{-16}$
J 1418+0718	$<1.7 \times 10^{-16}$	<71	$<2.6 \times 10^{-17}$
J 2205+1021	$<1.5 \times 10^{-17}$	<13	$<2.9 \times 10^{-17}$
J 2351–0639	$<5.5 \times 10^{-17}$	<26	$<4.2 \times 10^{-16}$
J 2359+1254	$<4.1 \times 10^{-17}$	<15	$<2.2 \times 10^{-17}$

^aStar formation rate estimated based on the line luminosity of $[\text{O II}] \lambda 3727$ following the calibration by Kennicutt (1998).

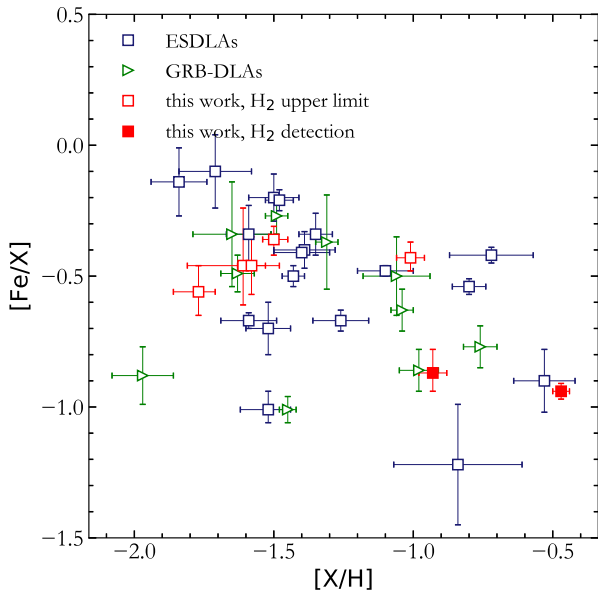


Figure 8. Metallicity versus iron depletion. ‘X’ corresponds to the volatile element Zn or S, depending on availability for each system. ESDLAs from this work are shown by open (H₂ upper limits) and filled (H₂ detections) red squares. Blue squares correspond to ESDLAs from Guimarães et al. (2012), Noterdaeme et al. (2015), and Ranjan et al. (2018, 2020). GRB DLAs from Bolmer et al. (2019) are shown by green triangles. The difference in the adopted solar abundances in the literature samples is within the metallicity uncertainties, so we do not address it here.

5 DISCUSSION

From the observed properties of individual ESDLAs towards quasar sightlines, it has been suggested that they arise from similar environments to DLAs observed from GRB afterglow spectra (Noterdaeme et al. 2015). Measurements based on about two dozen ESDLAs and a dozen GRB DLAs further support this idea (Bolmer et al. 2019; Ranjan et al. 2020). Therefore, subsequently we compare the properties of our seven systems with a sample of ESDLAs and GRB DLAs from the literature. Although our sample of ESDLAs is located in the same region in the metallicity-depletion diagram (Fig. 8),⁵ three of them have relatively high metallicities $[\text{Zn}/\text{H}] \gtrsim -1$ compared with the average of ESDLAs. We detected H₂ with $\log N(\text{H}_2) (\text{cm}^{-2}) > 18$ in those two systems with the highest depletion factor, which is consistent with the study by Ledoux,

⁵For the ESDLA system towards J 2246+1328 (Ranjan et al. 2020), we plot revisited metallicity and depletion from Ranjan et al. (2021).

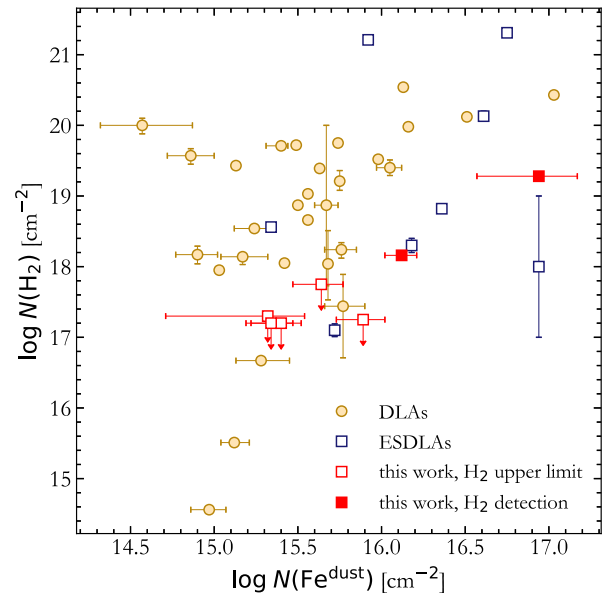


Figure 9. Column density of iron depleted into the dust versus H₂ column density. ESDLAs from this work are shown by red open (H₂ upper limits) and filled (H₂ detections) squares. Blue squares and brown circles are ESDLA and DLA systems, respectively, compiled in Balashev et al. (2019).

Petitjean & Srianand (2003). Since H₂ formation is connected with the amount of dust, one may expect a correlation between the H₂ column density with the column density of iron depleted into dust, i.e. the dust fraction (Noterdaeme et al. 2008a). In Fig. 9, we plot column densities of iron in the dust phase versus H₂ column densities. Our sample of ESDLAs is consistent with previous findings; i.e., the incidence rate of H₂ in DLAs gradually increases for systems with $\log N(\text{Fe}^{\text{dust}}) (\text{cm}^{-2}) > 15$ (Noterdaeme et al. 2008a; Balashev et al. 2019). Indeed, the two ESDLAs from our sample with strong H₂ absorption have the highest column densities of iron locked into dust, while the other five with upper limits on H₂ have $\log N(\text{Fe}^{\text{dust}}) (\text{cm}^{-2}) < 16$. While H₂-bearing systems with $\log N(\text{H}_2) (\text{cm}^{-2}) > 18$ exhibit a moderate correlation between H₂ and Fe^{dust} column density (Pearson correlation coefficient ≈ 0.4), the unknown selection functions do not permit a strict conclusion. Fig. 9 indicates that ESDLAs with H₂ detection have relatively high $N(\text{Fe}^{\text{dust}})$ in comparison with other H₂-bearing DLAs. This is evidently explained by the large columns probed by ESDLAs. ESDLA systems with large $\log N(\text{Fe}^{\text{dust}}) (\text{cm}^{-2}) > 16$ have much larger dispersion in the H₂–Fe^{dust} diagram, which could be due to a larger number of metal components with different physical conditions along the line of sight, whereas H₂ column densities are most probably determined on smaller scales, i.e. by local physical conditions. Since ESDLAs likely probe more central parts of the absorbing galaxies, the corresponding lines of sight are expected to cross regions with more diverse physical conditions than regular DLAs that probe predominantly the outskirts of galaxies, resulting in larger dispersion of integrated properties for ESDLAs.

6 SUMMARY

In this work, we have presented a detailed analysis of seven new ESDLAs. For all systems, we have estimated the H I column density, metallicity and dust depletion, dust extinction, and the column density of iron locked up in dust grains. For two out of seven, we

have detected strong $[\log N(\text{H}_2) (\text{cm}^{-2}) > 18]$ molecular hydrogen absorption. These two systems also demonstrate the highest column density of iron in dust grains, which indicates a significant integrated amount of dust in the corresponding systems. For the ESDLA towards J2359+1354, which has the strongest H_2 absorption and highest extinction A_V , we additionally detected neutral carbon, which is known to be a good tracer of H_2 , as well as Si II^* absorption, which may be used to estimate the electron density. Overall, the H_2 incidence rate of 10–55 per cent for ESDLAs in our sample is in agreement with the H_2 incidence rate observed in GRB DLAs (~ 30 per cent, Bolmer et al. 2019). This is significantly higher than the incidence rate of the overall population of intervening quasar DLAs (5–10 per cent).

Combining the sample presented in this work with the sample by Ranjan et al. (2020), we discuss the measurements of C II^* , which can be used to estimate the $[\text{C II}]$ cooling rate in the ISM. The distribution of the inferred cooling rates for our combined sample of ESDLAs presents the same bimodality as observed in DLA systems (Wolfe et al. 2008) with much smaller HI column densities (see Fig. 3). A more in-depth discussion of the origin of this bimodality is presented by Balashev et al. (2022).

In order to study the star formation activity in the absorbing galaxy, we have searched for emission lines from $[\text{O II}] \lambda 3727$ and $[\text{O III}] \lambda 5007$. We do not find any detections of these lines and report only upper limits to the line fluxes (assuming that the emission counterpart falls inside the slit aperture). The upper limits that we infer are rather high and in full agreement with the overall low star formation rates observed for ESDLAs with positive detections of the emission counterpart.

ACKNOWLEDGEMENTS

This work is partially supported by Russian Foundation for Basic Research (RFBR) grant 18-02-00596. KT and SB are supported by the Foundation for the Advancement of Theoretical Physics and Mathematics ‘BASIS’. We acknowledge support from the French Agence Nationale de la Recherche under ANR grant 17-CE31-0011-01/project ‘HIH2’ (PI: Noterdaeme) and from the French–Russian collaborative programme PRC 1845. AR acknowledges support from a National Research Foundation of Korea (NRF) grant funded by the Ministry of Science and ICT (NRF-2019R1C1C1010279). AR also acknowledges the support of the Indo-French Centre for the Promotion of Advanced Research (Centre Franco-Indien pour la Promotion de la Recherche Avancée) under contract no. 5504-2 (PIs Gupta and Noterdaeme) during the writing of the proposal for the ESO-VLT observations. JKK acknowledges support from the Swiss National Science Foundation under grant 185692. The authors are grateful to the European Southern Observatory (ESO) and in particular the Paranal Observatory’s staff for carrying out their observations in service mode.

DATA AVAILABILITY

The results of this paper are based on data retrieved from the ESO telescope archive. These data can be shared on reasonable request to the authors.

REFERENCES

Abolfathi B. et al., 2018, *ApJS*, 235, 42
 Albornoz Vásquez D., Rahmani H., Noterdaeme P., Petitjean P., Srianand R., Ledoux C., 2014, *A&A*, 562, A88

Anders E., Grevesse N., 1989, *Geochim. Cosmochim. Acta*, 53, 197
 Asplund M., Grevesse N., Sauval A. J., Scott P., 2009, *ARA&A*, 47, 481
 Balashev S. A. et al., 2017, *MNRAS*, 470, 2890
 Balashev S. A. et al., 2019, *MNRAS*, 490, 2668
 Balashev S. A., Ivanchik A. V., Varshalovich D. A., 2010, *Astron. Lett.*, 36, 761
 Balashev S. A., Noterdaeme P., 2018, *MNRAS*, 478, L7
 Balashev S. A., Petitjean P., Ivanchik A. V., Ledoux C., Srianand R., Noterdaeme P., Varshalovich D. A., 2011, *MNRAS*, 418, 357
 Balashev S. A., Telikova K. N., Noterdaeme P., 2022, *MNRAS*, 509, L26
 Bolmer J. et al., 2019, *A&A*, 623, A43
 Carswell R. F., Becker G. D., Jorgenson R. A., Murphy M. T., Wolfe A. M., 2012, *MNRAS*, 422, 1700
 Carswell R. F., Jorgenson R. A., Wolfe A. M., Murphy M. T., 2011, *MNRAS*, 411, 2319
 Cooke R. J., Pettini M., Jorgenson R. A., 2015, *ApJ*, 800, 12
 Dekker H., D’Odorico S., Kaufer A., Delabre B., Kotzlowski H., 2000, in Iye M., Moorwood A. F., eds, Proc. SPIE Conf. Ser. Vol. 4008, Optical and IR Telescope Instrumentation and Detectors. SPIE, Bellingham, p. 534
 Dutta R., Srianand R., Rahmani H., Petitjean P., Noterdaeme P., Ledoux C., 2014, *MNRAS*, 440, 307
 Ellison S. L., Pettini M., Steidel C. C., Shapley A. E., 2001, *ApJ*, 549, 770
 Fynbo J. P. U. et al., 2011, *MNRAS*, 413, 2481
 Goldoni P., Royer F., François P., Horrobin M., Blanc G., Vernet J., Modigliani A., Larsen J., 2006, in McLean I. S., Iye M., eds, Proc. SPIE Conf. Ser. Vol. 6269, Ground-based and Airborne Instrumentation for Astronomy. SPIE, Bellingham
 Goldsmith P. F., Langer W. D., Pineda J. L., Velusamy T., 2012, *ApJS*, 203, 13
 Gordon K. D., Clayton G. C., Misselt K. A., Landolt A. U., Wolff M. J., 2003, *ApJ*, 594, 279
 Guimarães R., Noterdaeme P., Petitjean P., Ledoux C., Srianand R., López S., Rahmani H., 2012, *AJ*, 143, 147
 Horne K., 1986, *PASP*, 98, 609
 Jorgenson R. A., Wolfe A. M., Prochaska J. X., 2010, *ApJ*, 722, 460
 Kennicutt Robert C. J., 1998, *ARA&A*, 36, 189
 Klimenko V. V., Balashev S. A., 2020, *MNRAS*, 498, 1531
 Klimenko V. V., Balashev S. A., Ivanchik A. V., Ledoux C., Noterdaeme P., Petitjean P., Srianand R., Varshalovich D. A., 2015, *MNRAS*, 448, 280
 Krogager J. K., Fynbo J. P. U., Noterdaeme P., Zafar T., Møller P., Ledoux C., Krühler T., Stockton A., 2016, *MNRAS*, 455, 2698
 Krogager J. K., Møller P., Fynbo J. P. U., Noterdaeme P., 2017, *MNRAS*, 469, 2959
 Kulkarni V. P., Meiring J., Som D., Péroux C., York D. G., Khare P., Lauroesch J. T., 2012, *ApJ*, 749, 176
 Lagache G., Cousin M., Chatzikos M., 2018, *A&A*, 609, A130
 Ledoux C., Petitjean P., Srianand R., 2003, *MNRAS*, 346, 209
 Levshakov S. A., Varshalovich D. A., 1985, *MNRAS*, 212, 517
 Milutinovic N., Ellison S. L., Prochaska J. X., Tumlinson J., 2010, *MNRAS*, 408, 2071
 Modigliani A. et al., 2010, in Silva D. R., Peck A. B., Sofier B. T., eds, Proc. SPIE Conf. Ser. Vol. 7737, Observatory Operations: Strategies, Processes, and Systems III. SPIE, Bellingham
 Møller P., Fynbo J. P. U., Fall S. M., 2004, *A&A*, 422, L33
 Noterdaeme P. et al., 2012a, *A&A*, 540, A63
 Noterdaeme P. et al., 2012c, *A&A*, 547, L1
 Noterdaeme P. et al., 2017, *A&A*, 597, A82
 Noterdaeme P. et al., 2021b, *A&A*, 651, A78
 Noterdaeme P., Balashev S., Krogager J. K., Laursen P., Srianand R., Gupta N., Petitjean P., Fynbo J. P. U., 2021a, *A&A*, 646, A108
 Noterdaeme P., Ledoux C., Petitjean P., Le Petit F., Srianand R., Smette A., 2007b, *A&A*, 474, 393
 Noterdaeme P., Ledoux C., Petitjean P., Srianand R., 2008a, *A&A*, 481, 327
 Noterdaeme P., Ledoux C., Zou S., Petitjean P., Srianand R., Balashev S., López S., 2018, *A&A*, 612, A58
 Noterdaeme P., López S., Dumont V., Ledoux C., Molaro P., Petitjean P., 2012b, *A&A*, 542, L33

- Noterdaeme P., Petitjean P., Ledoux C., López S., Srianand R., Vergani S. D., 2010, *A&A*, 523, A80
- Noterdaeme P., Petitjean P., Ledoux C., Srianand R., Ivanchik A., 2008b, *A&A*, 491, 397
- Noterdaeme P., Petitjean P., Pâris I., Cai Z., Finley H., Ge J., Pieri M. M., York D. G., 2014, *A&A*, 566, A24
- Noterdaeme P., Petitjean P., Srianand R., Ledoux C., Le Petit F., 2007a, *A&A*, 469, 425
- Noterdaeme P., Srianand R., Rahmani H., Petitjean P., Pâris I., Ledoux C., Gupta N., López S., 2015, *A&A*, 577, A24
- Pottasch S. R., Wesselius P. R., van Duinen R. J., 1979, *A&A*, 74, L15
- Rahmani H. et al., 2013, *MNRAS*, 435, 861
- Rahmati A., Schaye J., 2014, *MNRAS*, 438, 529
- Ranjan A. et al., 2018, *A&A*, 618, A184
- Ranjan A. et al., 2022, *A&A*, preprint ([arXiv:2201.06413](https://arxiv.org/abs/2201.06413))
- Ranjan A., Noterdaeme P., Krogager J. K., Petitjean P., Srianand R., Balashev S. A., Gupta N., Ledoux C., 2020, *A&A*, 633, A125
- Roy N., Frank S., Carilli C. L., Mathur S., Menten K. M., Wolfe A. M., 2017, *ApJ*, 834, 171
- Schlafly E. F., Finkbeiner D. P., 2011, *ApJ*, 737, 103
- Selsing J., Fynbo J. P. U., Christensen L., Krogager J. K., 2016, *A&A*, 585, A87
- Srianand R., Gupta N., Petitjean P., Noterdaeme P., Ledoux C., 2010, *MNRAS*, 405, 1888
- Srianand R., Gupta N., Petitjean P., Noterdaeme P., Saikia D. J., 2008a, *MNRAS*, 391, L69
- Srianand R., Noterdaeme P., Ledoux C., Petitjean P., 2008b, *A&A*, 482, L39
- Srianand R., Petitjean P., 2000, *A&A*, 357, 414
- Srianand R., Petitjean P., Ledoux C., Ferland G., Shaw G., 2005, *MNRAS*, 362, 549
- Telfer R. C., Zheng W., Kriss G. A., Davidsen A. F., 2002, *ApJ*, 565, 773
- Varshalovich D. A., Ivanchik A. V., Petitjean P., Srianand R., Ledoux C., 2001, *Astron. Lett.*, 27, 683
- Vernet J. et al., 2011, *A&A*, 536, A105
- Vladilo G., Bonifacio P., Centurión M., Molaro P., 2000, *ApJ*, 543, 24
- Watson D., 2011, *A&A*, 533, A16
- Wolfe A. M., Gawiser E., Prochaska J. X., 2005, *ARA&A*, 43, 861
- Wolfe A. M., Prochaska J. X., Gawiser E., 2003, *ApJ*, 593, 215
- Wolfe A. M., Prochaska J. X., Jorgenson R. A., Rafelski M., 2008, *ApJ*, 681, 881
- Zou S., Petitjean P., Noterdaeme P., Ledoux C., Krogager J. K., Fathivavsari H., Srianand R., López S., 2018, *A&A*, 616, A158

SUPPORTING INFORMATION

Supplementary data are available at *MNRAS* online.

Please note: Oxford University Press is not responsible for the content or functionality of any supporting materials supplied by the authors. Any queries (other than missing material) should be directed to the corresponding author for the article.

This paper has been typeset from a $\text{\TeX}/\text{\LaTeX}$ file prepared by the author.